Title

ICESat/GLAS Altimetry Measurements: Received Signal Dynamic Range and Saturation Correction.

Journal

IEEE transactions on geoscience and remote sensing : a publication of the IEEE Geoscience and Remote Sensing Society, 55(10)

ISSN

0196-2892

Authors

Sun, Xiaoli
Abshire, James B
Borsa, Adrian A
et al.

Publication Date

2017-10-01

DOI

10.1109/tgrs.2017.2702126

Peer reviewed

ICESat/GLAS Altimetry Measurements: Received Signal Dynamic Range and Saturation Correction

Xiaoli Sun, *Member, IEEE*, James B. Abshire, Adrian A. Borsa, Helen A. Fricker, Donghui Yi, John. P, DiMarzio, Fernando S. Paolo, Kelly M. Brunt, David J. Harding, and Gregory A. Neumann

***Abstract*—NASA's Ice, Cloud, and land Elevation Satellite (ICESat), which operated between 2003 and 2009, made the first satellite-based global lidar measurement of Earth's ice sheet elevations, sea-ice thickness and vegetation canopy structure. The primary instrument on ICESat was the Geoscience Laser Altimeter System (GLAS), which measured the distance from the spacecraft to Earth's surface via the roundtrip travel time of individual laser pulses. GLAS utilized pulsed lasers and a direct detection receiver consisting of a silicon avalanche photodiode (Si APD) and a waveform digitizer. Early in the mission, the peak power of the received signal from snow and ice surfaces was found to span a wider dynamic range than planned, often exceeding the linear dynamic range of the GLAS 1064-nm detector assembly. The resulting saturation of the receiver distorted the recorded signal and resulted in range biases as large as ~50 cm for ice and snow-covered surfaces. We developed a correction for this "saturation range bias" based on laboratory tests using a spare flight detector, and refined the correction by comparing GLAS elevation estimates to those derived from Global Positioning System (GPS) surveys over the calibration site at the salar de Uyuni, Bolivia. Applying the saturation correction largely eliminated the range bias due to receiver saturation for affected ICESat measurements over Uyuni and significantly reduced the discrepancies at orbit crossovers located on flat regions of the Antarctic ice sheet.**

***Index Terms*—satellite laser altimetry, laser ranging, lidar, remote sensing, ice sheets**

Manuscript received March 22, 2016; revised September 1, 2016 and February 21, 2017; accepted April 11, 2017. Date of publication xx.xx.xx; date of current version xx.xx.xx.

X. Sun, J. B. Abshire, and G. A. Neumann are with the Solar Exploration Division, National Aeronautic and Space Administration (NASA) Goddard Space Flight Center (GSFC), Greenbelt, MD 20771 USA (e-mail: xiaoli.sun-1@nasa.gov).

A. A. Borsa, H. A. Fricker, and F. S. Paolo are with the Scripps Institution of Oceanography, University of California San Diego, La Jolla, CA 92093 USA.

D. Yi and J. P. DiMarzio are with Stinger Ghaffarian Technologies (SGT) Inc., Greenbelt, MD 20770 USA.

K. M. Kelly is with the Earth System Science Interdisciplinary Center (ESSIC), University of Maryland, College Park, MD 20740 USA.

D. J. Harding is with the Earth Science Division, NASA GSFC, Greenbelt, MD 20771 USA.

I. Introduction

THE Geoscience Laser Altimeter System (GLAS) on board the Ice, Cloud, and land Elevation Satellite (ICESat) was the first orbiting space lidar to monitor Earth's polar regions for climate studies [1-3]. Launched on January 12, 2003, ICESat completed its mission in October 2009, and was de-orbited in August 2010 [4]. During its mission, GLAS made a total of 1.98 billion laser altimetry and atmospheric lidar measurements, and provided observations of Earth's surface elevation with unprecedented accuracy [5-7]. GLAS also served as a scientific and technical pathfinder for future orbiting lidar missions.

GLAS made estimates of surface elevations by measuring the range from the spacecraft to the Earth's surface using a 1064-nm Nd:YAG (neodymium:yttrium-aluminum garnet) laser, which was pulsed at 40 Hz. Three identical lasers were mounted on GLAS to provide redundancy and to extend the operational lifetime of the mission. Each laser pulse illuminated a 65-m diameter footprint on the surface, from which a small fraction of the incident laser energy was scattered back to the GLAS instrument and collected by the receiver telescope. The detector and the waveform digitizer recorded the time-varying optical power of both the outgoing laser pulse (the transmit pulse) and the reflected pulse from the surface (the return pulse, alternately referred to as the received pulse or echo). The range from ICESat to the surface was estimated from the time-of-flight, or travel time, of the laser pulse measured between these transmit and return pulses. In post-processing, the measured range was combined with the GPS-measured spacecraft position, the pointing direction of the laser beam, and corrections for atmospheric effects to derive the geodetic coordinates (latitude, longitude) and elevation of each ICESat laser footprint.

The primary purpose of GLAS was to measure surface elevation changes along satellite ground tracks over Antarctica and Greenland. The environmental conditions in these regions varied widely with location and time, resulting in considerable variability in the peak optical power of the return pulses. Weak signals were often received from coastal regions due to the attenuation from clouds. Much stronger signals were received when the atmosphere was clear and the surface

reflectance was high, conditions that typically occurred at high elevations on the Antarctic and Greenland ice sheets. Additionally, there was a general loss in transmit energy over time for each of the three lasers due to aging of the laser components. To conserve laser life, ICESat was operated in a series of campaigns (Table I). The laser energy, and thus the peak power of return pulses, was higher in the earlier campaigns for each laser.

Due to the importance of measuring elevation changes near the Antarctic and Greenland margins, the laser energy and receiver telescope diameter of the GLAS instrument were chosen to ensure that return pulses could be detected even with some attenuation of pulse energy in the presence of clouds. These choices increased the sensitivity of GLAS to all return pulses and helped to maintain nominal instrument operation as the transmitted laser pulse energy decreased over time. However, under high signal conditions (high energy, high reflectance and clear sky), the peak power of the return pulse sometimes exceeded the GLAS receiver's linear dynamic range and caused receiver saturation. This resulted in distorted return pulse waveforms that exhibited flattened peaks and delayed trailing edges, with the width of the waveform proportional to total received energy. When processed by the original ranging algorithms, which were based on the assumption of a linear receiver response to received power, these waveform distortions resulted in longer laser pulse travel times and correspondingly lower surface elevations (i.e. a positive range bias). This effect was discovered during the first few campaigns of the ICESat mission [2,6].

Laboratory testing using a spare flight detector with a laser pulse shape similar to GLAS showed that the range bias due to receiver saturation could be modeled as a function of return pulse energy for constant pulse width. Using results from these tests, we developed a preliminary saturation correction early in the mission [8]. This algorithm significantly improved GLAS surface elevation measurements [9] and was implemented in GLAS data processing software for data product Release 24 [September 2005] and was incrementally improved in Releases 26 [January 2006] and 28 [September 2006]. A description of all ICESat/GLAS data product releases is available in [10]. Subsequently, we refined the algorithm by comparing actual GLAS-derived elevations to a GPS-derived digital elevation model (DEM) of the GLAS calibration site at the salar de Uyuni, Bolivia. Saturation corrections based on the refined algorithm first appeared in Release 33 [March 2011] and passed unchanged into the final release of the dataset, Release 34 [May 2014]. We also developed a saturation correction algorithm for the return pulse energy that was available in Release 428 and higher, though the results were not as thoroughly tested as those for the saturation correction algorithm for range.

In this paper, we describe the cause of the GLAS detector saturation and the evolution of the saturation correction algorithm. We begin with an overview of the GLAS 1064-nm receiver design, the signal dynamic range of the return pulses, the nature of receiver saturation, and the characteristics of saturated signals from flat ice sheet surfaces. We then describe the laboratory test results and how they were used to develop the saturation correction algorithm. We also discuss the validation and refinement of the saturation correction algorithm by comparing corrected and uncorrected GLAS elevations with the GPS reference surface at the salar de Uyuni, Bolivia. Finally, since the correction is included with, but not applied to, the data available from the NASA archive at the National Snow and Ice Data Center (NSIDC), we discuss how users can apply the saturation correction to ICESat/GLAS data for their own research.

II. GLAS ALTIMETRY RECEIVER DESIGN AND DYNAMIC RANGE

A. GLAS Receiver Design

The GLAS lidar utilized three nearly identical Q-switched Nd:YAG lasers, which were operated sequentially during the ICESat mission. The GLAS lasers were designed to transmit 6-ns wide pulses at a rate of 40 Hz. Initially, each laser had a pulse energy of about 70 mJ, which declined over time. The GLAS receiver used a 1-meter diameter telescope to collect surface-reflected return pulses, feeding the received signals through a series of amplifiers and into a waveform digitizer. The lowest transmit pulse energy that could be used to make useful measurements was 5-10 mJ/pulse, depending on the surface reflectance, surface roughness and atmospheric conditions. Table II lists these and other relevant GLAS instrument design parameters [6,11].

The GLAS detector assembly converted the optical power of each return pulse into a waveform (of voltage versus time), which was digitized and recorded. The detector assembly utilized a silicon avalanche photodiode (Si APD) and preamplifier module, a buffer amplifier, a variable gain amplifier (VGA), and two linear amplifiers (Fig. 1). The VGA gain was adjusted on every shot via an automatic gain control (AGC) loop. The gain value chosen by the control algorithm ensured that: a) the detector dark noise at the highest VGA gain was several times the waveform digitizer noise floor, so that the detector dark noise remained the dominant noise source; b) the average peak amplitude of the weakest return pulses spanned at least 1/4 of the 256-step range of the waveform digitizer, so that the waveform digitizer quantization error was negligible when determining the return pulse arrival time for time-of-flight measurement; and c) the combined amplifier response remained linear over the entire signal and gain range.

The AGC was implemented in on-board software as a second-order loop filter, and the AGC gain value was updated for every laser shot. The average pulse amplitude was maintained at about 50% the full range of the waveform digitizer, and the loop filter parameters were chosen to give the fastest response without oscillation. For small (<50%) changes in the input signal amplitude, the average control loop response time was about 0.1 sec (adjustment within 3 to 4 laser shots). For large (e.g. factor of 10) changes in the signal amplitude, the response time was about 0.25 sec (10 laser

shots). The same AGC algorithm was used for all three lasers in all campaigns, except for Laser 1 during GLAS initial operation in orbit.

The detector assembly was designed to maintain a linear response between its output voltage and the optical power of the return pulse. In practice, all signal amplifiers in the detector electronics circuit had finite linear dynamic ranges. Saturation occurred when the peak voltage exceeded the linear dynamic range of one or more amplifiers, causing distortions in the return pulse waveforms and, therefore, biases in the surface elevation measurement. In the GLAS receiver design, the gain values of the amplifiers were chosen so that all the amplifiers reached the maximum in their dynamic range at the same time as the overall system dynamic range reached a maximum. The waveform digitizer was scaled to have a slightly higher saturation threshold so that it could capture the onset of amplifier saturation for characterization and potential correction in ground data processing.

Return pulse width was an important factor determining the peak power of the return pulse, since for a given energy level, narrower pulses had higher peak powers than broader pulses. The smallest return pulse widths (~6 ns) were obtained over smooth surfaces whose surface normal was oriented parallel to the incoming laser beam. Increases in apparent surface slope (the angle between the surface normal and the pointing direction of the laser) resulted in a non-linear increase in pulse width [13] [14] (Fig. 3).

To avoid detector damage from strong specular reflections, the GLAS laser beams were pointed away from nadir by 0.32–0.48°, which increased the nominal minimum return pulse width from 6 ns to 6.2-6.4 ns FWHM (full width at half maximum; Fig. 3). In the center of the Antarctic Ice Sheet, where surface slopes are less than 0.1°, off-nadir pointing was the primary source of this "pulse broadening." Within 300 km of the coast, however, surface slopes are much larger and were the dominant source of return pulse broadening.

B. Expected GLAS Receiver Signal Dynamic Range

GLAS was designed to accommodate return pulses over a broad range of signal power, with the lower and upper bounds of that range pre-defined using assumptions about laser performance, atmospheric transmission, and surface reflection. The weakest returns were expected from the periphery of the Antarctic and Greenland ice sheets, where we assumed 60% surface reflectance [15], 3° surface slope, and optical transmission typical of cirrus clouds (t_{atm} = 22%, or 1.0/km optical depth and 1.5 km thickness [16]). Under these assumptions, the return pulse at maximum transmitted laser energy would have a pulse energy of 0.29 fJ and a pulse width of 15 ns FWHM, corresponding to 19 nW peak optical power. The strongest returns were expected from the central Antarctic ice sheet under clear sky conditions. Assuming flat surfaces and one-way atmosphere transmission of 70%, the return pulse at maximum transmitted laser energy would have a return pulse energy of 9.5 fJ and a pulse width of 6 ns FWHM, corresponding to 1.6 μW peak optical power. The expected dynamic range of peak power between the strongest and weakest return signals was therefore estimated to be 80-90.

The GLAS receiver's linear dynamic range was designed to cover the expected signal dynamic range with a margin of safety. Within the GLAS receiver, the VGA's adjustment range from lowest to highest gain was at least a factor of 30. The waveform digitizer had an additional dynamic range of 4 by scaling the weakest measurable signal amplitude to 1/4 of the maximum input level. The Si APD preamplifier module had a slightly wider linear dynamic range, and was not a limiting factor in the overall dynamic range. With all these components operating nominally, the GLAS detector assembly had a maximum linear range up to 13 fJ for 6 ns pulses, corresponding to a peak power of 2.2 μW. This provided a 38% margin above the expected maximum peak power (1.6 μW).

It was anticipated that received power would exceed the design maximum only over specular surfaces such as shallow lakes. Since specular returns were expected to occur infrequently, it was decided that the receiver only needed to survive the spike in peak power from specular returns, but did not need to provide precise range measurements for those pulses. Data from the detector manufacturer showed that the maximum non-damaging received signal power was 2.1 mW, which corresponded to a 13 pJ/pulse received pulse energy for a 6-ns laser pulse width. Given this limit, and assuming a ~0.02 Fresnel reflectivity of water and a uniform distribution of reflected laser light within a cone whose diameter was twice the off-nadir angle, we determined that the laser had to be continuously pointed off nadir by >0.3° in order to avoid detector damage from specular returns, consistent with the actual off-nadir pointing angles chosen for the mission.

C. Observed On-Orbit Signal Dynamic Range and Saturation Effects

On orbit, variations in laser transmit energy, environmental conditions, and surface reflectance occasionally caused the return pulse energy to exceed the receiver linear dynamic range, resulting in saturation of the GLAS receiver for some measurements. The degree of receiver saturation (parameter "d_pctSAT" in the ICESat data products) is reported for every shot and is calculated as the percentage of the signal portion of the waveform that exceeds a specified saturation threshold (parameter i_satNdx, given in waveform digitizer counts).

Saturation effects were most prevalent early in the mission over the interior of the East Antarctic Ice Sheet when skies were clear and laser transmit energies were high. The two-way atmosphere transmission appeared to be twice what we had assumed and the surface reflectivity (ρ_{sur}) appeared 1.5 times higher than we had assumed over most of this region [17-19]. For example, return pulse energies during campaign Laser 2a varied between 20 and 30 fJ (Fig. 2), exceeding the upper end of the detector's linear dynamic range by a factor of 2 to 3.

Even stronger signals were recorded from water surfaces such as in the Everglades National Park in Florida, where return pulse energies reached 80 fJ. The strongest return pulse energies were recorded during campaign Laser 3b at the salar de Uyuni, Bolivia, where a shallow layer of water over a dry lake bed led to the specular reflection of laser energy back to

the GLAS telescope. We later reproduced the waveform shape using the spare detector in the lab and estimated the return pulse energy to be about 1000 fJ, or 1/10 of the detector damage level.

Receiver saturation caused a characteristic distortion of the GLAS return pulse waveform, which can be seen clearly in returns from the salar de Uyuni, Bolivia (Fig. 4). Because the salar surface is flat, smooth and stable over time, observed differences in waveform shape can be primarily attributed to saturation. Under nominal conditions with no saturation, salar returns were similar to the transmit pulse (i.e. narrow and Gaussian). Mild saturation (1-10% saturation index in the data product) resulted in clipped waveform peaks and slightly widened pulses, while stronger saturation generated tabular waveforms that grew wider as saturation increased. Since GLAS used the centroid of the Gaussian fit to the return waveform to determine the arrival time of the return pulse, saturation had a direct impact on the GLAS range measurement. Specifically, as saturation widened and distorted the return waveform, the centroid of the Gaussian fit moved further from the waveform leading edge, resulting in a delayed return pulse arrival times, longer range measurements, and lower elevation estimates. This effect, which is apparent in the Gaussian fits to the return waveforms in Fig. 4, exceeded 2 m in the most extreme cases.

III. DEVELOPMENT OF THE SATURATION CORRECTION ALGORITHM

We conducted a series of laboratory tests from 2004 to 2005 using the spare flight detector assembly (Fig. 5) to reproduce saturation-distorted return pulse waveforms and provide calibration data for the development of a saturation range bias correction. We generated test waveforms using a 1060-nm wavelength laser diode that was modulated by an arbitrary waveform generator to produce a Gaussian-like pulse shape with 6 ns FWHM pulse width. The detector response at 1060 nm was nearly identical to that at 1064 nm, and the difference in the responsivity was accounted for in the signal calibration.

A portion of the laser signal was split off and focused onto a high-speed photodiode to simulate the transmitted laser pulse and to trigger the oscilloscope. The oscilloscope triggering time was used as the starting reference time for the laser pulse arrival time measurement (T_{ref}) from which the laser range was derived. In this setup, the starting reference time corresponded to the leading edge of the transmitted pulse waveform rather than the centroid of the Gaussian fit to the transmit waveform (which was how the GLAS return pulse was actually timed). This did not impact our analysis since the transmit pulse shape and amplitude were held constant throughout the laboratory tests so that the only changes in range were due to changes in the return waveform shape.

In order to simulate return pulses with different energies, the laser diode power was adjusted using an optical fiber attenuator and monitored with an optical power meter. The laser output was fed into a multimode optical fiber, delayed, attenuated, and focused onto the detector. The output of the detector was connected to an oscilloscope that had the same resolution (8 bits) and sampling rate (1 GHz) as the GLAS waveform digitizer. We used a power supply to control the VGA gain, with the control voltage scaled to match the GLAS VGA control telemetry (i.e. 0 corresponded to the minimum control voltage and 255 corresponded to maximum control voltage).

A. Laboratory Test Results

We recorded output ("return") pulse waveforms from the detector assembly over a range of input ("transmit") pulse energy levels and VGA gains. At the minimum VGA gain setting (13) used for most of the GLAS campaigns, the receiver became saturated when output pulse energies exceeded 13 fJ, producing waveforms with flattened peaks and increased pulse width (Fig. 6). These waveforms were similar to those observed from GLAS on orbit, with a notch at the top of the waveform near its trailing edge. The output waveform width increased monotonically with received energy (to as much as 50 ns), as did the total area under the waveform.

For each of the input energy levels we tested, we fit Gaussian curves to the output waveforms using the GLAS ground data processing algorithms. We then calculated the pulse travel time t_{tof} for each pulse by subtracting the oscilloscope reference time T_{ref} from the time T_G associated with the peak of the Gaussian (i.e. $t_{tof} = T_G - T_{ref}$). For each pulse we then estimated a saturation "travel time bias" δt_{tof} by subtracting the average travel time $\overline{t_{tof}}$ for a representative set of unsaturated pulses from t_{tof} (i.e. $\delta t_{tof} = t_{tof} - \overline{t_{tof}}$).

For VGA gain 13 and input energy between 15 fJ and 160 fJ, we found that the travel time bias increased monotonically with return pulse energy (Fig. 7). We repeated this test for a range of detector VGA gain settings and found that in each case the travel time bias increased linearly with pulse energy, but at different rates for different VGA gain values. Additionally, the pulse energy at which saturation initiated generally decreased with increasing VGA gain (Fig. 8). We also found that for each VGA gain, saturation started to occur at a specific value of the 256-step digitized waveform (Fig. 9). This "saturation threshold" (the parameter i_satNdx introduced in Section II.C) was defined by the following piecewise curve:

$$y_{th} = \begin{cases} 3826.9 + 9286.1 \times \log_{10}(G) \\ -7088.1 \times \log_{10}^2(G) + 1806.0 \times \log_{10}^3(G), & G \le 30 \\ 238 & G > 30 \end{cases} \quad (1)$$

where yth is the saturation threshold amplitude given in waveform digitizer units (0–255) and G is the VGA gain setting.

The laser pulse energies estimated from the Gaussian fit of the return pulse waveforms were also biased when the detector was saturated, especially for high values of VGA gain (Fig. 10). Appendix A describes an algorithm for correcting return pulse energies for saturation.

B. Development of the Saturation Correction Algorithm

The laboratory test results showed that the travel time bias

due to saturation could be estimated from the Gaussian fit to the return pulse waveform for any VGA gain setting, provided that surface slopes were small and the actual return pulse width was nearly unchanged. Using the data shown in Figure 8, we were able to approximate the travel time bias curves by:

$$\delta t_{tof}(E_r, G) = a_0 ln\left[1 + b_0 exp\left(\frac{E_r - E_{th}(G)}{\alpha(G)}\right)\right], \quad (2)$$

where E_r is the return pulse energy calculated from the Gaussian fit, G is the VGA gain setting, and $E_{th}(G)$ is the threshold energy at the onset of saturation for a given G. The constants $a_0 = 0.25$ and $b_0 = 0.0625$ control the rate of change of δt_{tof} in the vicinity of $E_{th}(G)$ and were determined from a fit to the measurements. The parameter $\alpha(G)$ controls the slope of the travel time bias versus received energy after saturation. The functions $E_{th}(G)$ and $\alpha(G)$ are approximated as

$$E_{th}(G) = c_1 + \frac{c_2 \frac{G}{c_3}}{\sqrt{\left(\frac{G}{c_3}\right)^{c_4} + c_5}}, \quad (3)$$

$$\alpha_{th}(G) = c_6 + \frac{c_7 \frac{G}{c_8}}{\sqrt{\left(\frac{G}{c_8}\right)^{c_9} + c_{10}}} \quad (4)$$

where c_1 through c_{10} are constants determined from the test data. An example fit to the travel time bias curve for VGA gain 13 is shown in Fig. 7 with $E_{th}(13) = 10.05$ and $\alpha(13) = 1.516$.

Fig. 11 shows the surface defined by (2)-(4), with the coefficients of the model listed in the second column in Table V. The difference, or misfit, between this surface model and the test data from which it was derived was <6 cm for return energies of 1–40 fJ/pulse for all gain values. For VGA gain 13, which was the gain value for most of the saturated data, the maximum difference between the surface model and test data was <2 cm for pulse energies of 0–40 fJ and <7 cm for pulse energies from 40–140 fJ.

We converted the travel time bias from (4) to a range bias by multiplying by $c/2$, with c the speed of light, and generated a range bias look-up table for each VGA gain/energy combination. This table summarized our preliminary range correction for saturation, which was valid for surface slopes <0.5°.

IV. EVALUATION AND REFINEMENT OF THE SATURATION CORRECTION AT THE SALAR DE UYUNI, BOLIVIA

To evaluate the saturation range bias correction presented in Section III, we compared the saturation-corrected surface elevations with "ground truth" obtained from independent GPS surveys of the ICESat calibration site at the salar de Uyuni in Bolivia [9]. In this section we describe the surveys and the use of the ground-truth data to validate and refine the saturation correction.

A. Salar de Uyuni GPS surveys

The salar de Uyuni in Bolivia (latitude 20.0°S, longitude 67.5°W) is the largest salt flat on Earth. A 54 x 45 km section of the salar was surveyed at the end of the dry season in September 2002 using car-mounted dual-frequency GPS receivers [9] [20]. From the GPS elevation data, we generated a local Digital Elevation Model (DEM) with an absolute accuracy better than 2.2 cm RMSE (root mean square error) [20; Fig. 12]. A repeat of the GPS survey was conducted in November 2009 [21] to assess potential elevation changes over the seven-year period and found changes of up to several cm within the survey area.

ICESat/GLAS operated between 2003 and 2009, within the period spanned by these two GPS surveys. To generate reference elevations for ICESat, we assumed that surface changes between 2002 and 2009 (Fig. 12b) were linear in time and interpolated the surface elevations to the epoch of each ICESat/GLAS pass. This assumption of linear change is consistent with surface deformation estimates we made for the salar de Uyuni using interferometric synthetic aperture radar (InSAR) processing of ALOS (Advanced Land Observing Satellite) data. Analysis of these interferograms showed that there was no seasonal signal and increasing average surface deformation with time [22].

B. ICESat/GLAS Measurements over the salar de Uyuni

Two ICESat/GLAS ground tracks crossed the salar de Uyuni survey area: Track 85 (descending) and Track 360 (ascending) (Fig. 12). Repeated measurements along these tracks were acquired during each ICESat campaign, and under clear sky conditions both tracks yielded more than 300 individual elevation observations per campaign over the survey area.

Receiver saturation occurred during many of the ICESat passes across the salar de Uyuni due to high surface reflectance (diffuse reflectance values of 50–90%) and generally clear atmospheric conditions. A shallow water layer was occasionally present on the salar, leading to specular returns and pulse energies that were orders of magnitude higher than observed for dry conditions, causing severe saturation. Except when it was completely flooded, the salar provided a nearly ideal test surface for the saturation correction algorithm, especially for passes that contained both saturated and unsaturated returns [9]. Fig. 13 shows an example of data from a single pass over the salar on Track 360 under clear sky conditions, with patches of water on the surface. The recorded waveforms exhibited a range of peak clipping and pulse broadening, indicating varying degrees of receiver saturation.

To obtain calibration data across a range of VGA gain values, we set the VGA gain for Track 360 from campaign Laser 3e onwards to different constant values (Table III). The VGA gain for Track 85 continued to be automatically adjusted by the control loop, but due to the high albedo and clear skies at Uyuni, most of the Track 85 data were collected at the preset lower VGA gain limit of 13.

C. Using the salar de Uyuni Reference Surface to Refine the GLAS Saturation Correction

There were 34 ICESat/GLAS passes over the salar de Uyuni during the 6.5-year ICESat mission. From the 15 passes containing saturated return waveforms, we chose 7 to validate the saturation correction algorithm (Table III), focusing on passes that contained both saturated and unsaturated waveforms to allow us to isolate the range bias due to receiver saturation alone (see discussion below). For each GLAS footprint, we obtained the corresponding reference elevation by interpolating the two GPS DEMs in both space (bilinear interpolation between nodes of the DEM grid) and in time (linearly interpolating between the values of the 2002 and 2009 DEMs at the GLAS footprint location). We then differenced the GLAS and reference elevations to obtain the elevation misfit.

Differences between ICESat elevations and the DEM occurred even when the receiver was not saturated, a result that has been reproduced by various investigators under a broad range of surfaces and conditions (see Fig. 19 and discussion on intercampaign biases in [23]). For example, there was an average of –0.034 m range bias (i.e. ICESat elevations were on average 3.4 cm higher than the DEM) for unsaturated return pulses on Track 360 in campaign Laser 3b (Fig. 14). We attribute biases in unsaturated pulses to sources such as unmodeled atmospheric delay, pointing knowledge biases and orbit determination errors, which we assume were constant during each 8-second Uyuni overflight. To develop the saturation correction, we excluded non-saturation error sources by using data from only the passes with both saturated and unsaturated return pulse waveforms. This allowed us to reference the misfit of the saturated pulses to the average misfit of the unsaturated pulses to produce a range bias that we assumed was due to saturation only.

We first considered the range bias versus return pulse energy at the salar de Uyuni for return pulses with VGA gain 13 only (Figure 15a). To model the saturation range bias for these pulses, we used the same functional form we introduced for the laboratory tests given in (4), which is parameterized by threshold received energy $E_{th}(G)$ and the slope $\alpha(G)$ of the range bias vs. received energy curve. We fit Equation (4) to the elevation misfit and obtained parameter values of $E_{th}(13) = 9.0$ and $\alpha(13) = 1.33$. In a similar manner, we determined the elevation misfit curves for return pulses with VGA gains 26, 80, and 125 (Table IV; Fig. 15b).

Using these empirical values from Table IV, we derived new constants for (5) and (6) (Table V) which, together with (4) defined a "refined" saturation correction for all values of G and E_r. This saturation correction had to be bounded to exclude extreme cases, and we used data from the salar de Uyuni to generate upper limits on the correction (Fig. 16). Because data were only available for a few gain values, we used linear interpolation to determine the upper bound for other gain values.

The refined saturation correction was implemented in Release 33 as a lookup table for all observed values of received energy and VGA gain over the ICESat mission. Application of the refined correction significantly reduced the elevation error between GLAS and the GPS DEM. For the 7 ICESat passes over the salar de Uyuni that were used to refine the saturation correction algorithm (Fig. 17), the elevation misfits were 0.6±3.1 cm (1σ) for VGA gain 13, 1.5±4.5 cm for VGA gain 13 to 40, and 2.5±7.5 cm for VGA gains 40–128, excluding specular returns. The larger error values for VGA 40–128 reflect the sparser validation data available for curve fitting at higher gains. For severely saturated returns from specular reflections of the flooded salar surface, the misfit was reduced from ~130 cm to -5.7±3.3 cm. For all the ICESat passes over Uyuni with VGA gain ≤ 20 (58% of the total), the misfit was reduced from -4.2±6.2 cm without saturation correction to 0.0±3.4 cm with the saturation correction.

The refined saturation correction was used in Release 33 and Release 34 for Laser 3 data only, while the laboratory correction was used for Lasers 1 and 2. The reason the laboratory correction was used for Laser 1 was that its minimum VGA gain was 8 (vs. 13 for Lasers 2 and 3), which was outside the range of VGA gain values in the salar de Uyuni test data. Laser 1 pulses were also wider than those of Laser 3 (Fig. 18) and more similar to those from the laboratory test setup. In the case of Laser 2, we have already shown that the laboratory-derived algorithm gives satisfactory results for VGA gain 13 without additional refinement [9]. Since there were no saturated Laser 2 salar de Uyuni data with VGA gain higher than 13, the laboratory algorithm was sufficient for Laser 2.

V. Discussion

A. Evaluation of the Saturation Correction over the East Antarctic Ice Sheet

We evaluated the effectiveness of the saturation correction over flat areas (slope < 0.05°) of the East Antarctic Ice Sheet via the analysis of crossover elevation biases using Release 634 data, both with and without the Gaussian-Centroid (GC) range correction described in [23]. We calculated crossover differences between all tracks with respective to a reference campaign, Laser 3j, which experienced no saturation due to its low laser transmit energy. This yielded approximately 1500 crossovers per campaign (after applying a 3-sigma iterative filter). We examined four different scenarios: a) no corrections applied; b) GC correction applied; c) GC and laboratory-determined saturation correction applied; and d) GC and refined saturation correction from the previous section applied. The results are shown in Fig. 19.

The saturation corrections have the greatest effect on crossover biases for campaigns Laser 2a and Laser 3a through Laser 3d, which were the campaigns with the highest laser transmit energies. The application of the GC correction has the biggest effect for Laser 2 and the first three campaigns of Laser 3, although the magnitude of the effect (ranging up to 10 cm) is generally much smaller than that of either saturation correction (ranging up to 40 cm). The saturation correction algorithm derived from the laboratory tests tends to

undercorrect the range biases due to saturation compared to the refined algorithm based on the salar de Uyuni measurements. The refined saturation correction and the GC correction removed the two major known artifacts of the GLAS instrument and data analysis. The resultant crossover differences from all the campaigns with respect to Laser 3j varied by a few cm, which was within the ICESat mission requirement.

B. Limitation over Sloped Surfaces

A limitation to the accuracy of the saturation correction formula is the surface slope. The return pulse waveforms are the convolution of the transmitted waveform with the impulse response of the surface in the direction of the laser pointing angle. Large surface slopes broaden the echo waveforms, which reduces their peak power. For a combined surface slope and off-nadir pointing angle of less than 0.5º, the return laser pulse can be assumed to be unchanged and the saturation correction applied as above. We also found that the saturation correction reduces range error for surface slopes from 0.5 to 1º, but for slopes greater than 1º the algorithm over-corrects the range, resulting in anomalously high surface elevations.

We conducted several laboratory experiments using wider laser pulses to simulate the returns from sloped surfaces. Results from these experiments suggest that the saturation correction algorithm could be modified to include the effect of surface slope, provided one could estimate the local slope by independent means. We did not pursue this investigation since the majority of saturated signals during the ICESat mission came from nearly flat surfaces.

There are a few cases where the saturation correction should not be applied: a) where surface slope > 7º; b) where pulse width > 50 ns, which was beyond the limit of pulse widening due to saturation; and c) for returns whose parameters exceeded the upper gain/energy bound defined by the points (gain, energy) = (250, 4 fJ), (25, 45 fJ), and (13, 100 fJ).

C. Applying the Saturation Correction to ICESat Data

Saturation corrections have been available since Release 24 of the ICESat dataset, but the form and content of the correction has changed over time. In all cases, the saturation correction is not automatically applied to the derived elevations, but is provided as a separate parameter that must be *added* to ICESat elevations by the user.

For historical reference, we note that in Release 24, the saturation correction from laboratory tests for gain value 13 was provided as parameter d_satRngCorr in data products GLA06 and GLA12–GLA15. It was meant to be added to elevation estimates or (if needed) subtracted from range estimates for all GLAS returns which had their saturation flag parameter i_satCorrFlg set to one. In Release 26, the saturation correction was extended to returns with all gain values based on the laboratory test data. Return pulses whose amplitude exceeded the saturation threshold for any applied VGA gain were flagged as saturated, and the saturation correction was meant to be applied by the user in the same way as for Release 24.

From Release 28 onward, the saturation correction was renamed to d_satElevCorr to properly reflect its sign convention. The correction is zero when returns are unsaturated, non-zero when returns are saturated, and undefined when a saturation correction is needed but the algorithm is not defined (e.g. for large saturation corrections). Updates to the saturation correction using calibration data from the salar de Uyuni continued through Release 633, but current users of ICESat data should use Release 634 if possible, since it incorporates several final improvements in the dataset.

The specific data products relevant to this discussion are GLA06 (Global Elevation Data), GLA12 (Antarctic and Greenland Ice Sheet Altimetry data), GLA13 (Sea Ice Altimetry Data), GLA14 (Global Land Surface Altimetry Data), and GLA15 (Ocean Surface Altimetry Data). Each product targets a different user community, but all contain the same saturation correction parameter (d_satElevCorr) which must be added to ICESat elevations (d_elev).

D. Remaining sources of error in ICESat Data after Saturation Correction

The saturation correction algorithm described here compensates for a known characteristic of the GLAS receiver. There are additional sources of cm-level errors in GLAS elevation data, some of which have been identified along with the corrections (e.g. the G-C error [23]) and others that were not well understood and uncorrected. These include range biases caused by blowing snow [24], unmodeled atmospheric delay, laser beam pointing biases, and uncertainties in the satellite orbit. Future work should focus on identifying these error sources and on making additional improvements to the ICESat dataset.

VI. SUMMARY

The GLAS instrument on the ICESat mission encountered a wider range of return pulse energies than anticipated. When laser energies were high, the detector output became distorted (“saturated”) when measuring flat bright reflective surfaces such as high-elevation ice-sheet areas through a clear atmosphere. Processing these distorted return waveforms using the standard GLAS ranging algorithm resulted in range and surface elevation biases of several tens of cm for ice sheets and up to 150 cm for specular water surfaces. Because this effect was caused by a reproducible non-linear response in the detector assembly, the resulting range bias could be modeled for flat surfaces, which allowed us to develop a saturation correction for range and surface elevation measurements. We conducted a series of laboratory tests using a spare flight detector assembly and a test laser to reproduce saturated pulse waveforms and estimate the range bias due to saturation. We generated a saturation correction algorithm based on the laboratory test data and used it in the early releases of the GLAS data products. The coefficients of the saturation correction algorithm were later updated by comparing GLAS elevations to a GPS-derived digital elevation model (DEM) at the salar de Uyuni, a large ICESat/GLAS calibration surface in Bolivia. The saturation

correction algorithm was shown to be effective, largely eliminating the range bias caused by receiver saturation for most of the ICESat measurements over Uyuni, and significantly reducing the crossover discrepancies for the flat regions of the Antarctic ice sheets.

APPENDIX: SATURATION CORRECTION FOR THE GLAS RETURN PULSE ENERGY FOR SURFACE REFLECTANCE MEASUREMENTS

The GLAS surface return pulse energy is determined by the transmitted pulse energy, surface reflectivity, surface scattering properties and atmospheric transmittance, and can be calculated from the lidar equation [12], as

$$E_{echo} = E_{tx}\eta_{rcvr}\frac{A_{rcvr}}{R^2}\cdot\frac{\rho_{sur}}{\Omega}\tau_{atm}^2 \quad \text{(A1)}$$

where E_{echo} is the return pulse energy, E_{tx} is the transmitted pulse energy, η_{rcvr} is the receiver optics transmission, A_{rcvr} is the receiver telescope area, R is the range to the target, ρ_{sur} is the surface reflectivity, Ω is the equivalent scattering solid angle, and τ_{atm} is the one-way atmosphere transmittance, For Lambertian surfaces such as desert, Ω = π. For specular reflection from smooth water surfaces Ω can be very small, which results in high lidar return pulse energies from locations like flooded salar de Uyuni and the Everglades.

The GLAS ground based algorithms calculated the return pulse energies by integrating the Gaussian fit to the digitized pulse waveform to determine pulse area. The apparent surface reflectance was derived using the lidar equation (1),

$$T_{\rho\tau\tau} = \rho_{sur}\frac{\tau_{atm}^2}{\Omega/\pi}. \quad \text{(A2)}$$

When the atmosphere transmission and scattering solid angle were known through independent means, the surface reflectance could be solved. GLAS measured the surface reflectance at zero phase angle, for which the direction of the illumination and the observation were opposite of each other. The measurements in this case were influenced by specular reflection and by the opposition effect [25].

The GLAS receiver used the same detector and electronics to record the transmitted and the return laser pulse waveforms. The pulse energies for both the transmitted and the return pulses could be computed from the digitized pulse waveforms using the same equation but different parameter values, as

$$E_g = \frac{\alpha}{\eta_e\eta_o R_{Det} G}\sum_{i=1}^{N} v_w(i)\Delta t_s \quad \text{(A3)}$$

where E_g represent either the transmitted or the received laser pulse energy, α is a calibration constant, η_e = 92.3% is the electronic throughput, η_o is the optical throughput, R_{Det} = 2.28 × 10^7 V/W is the detector responsivity, G is the VGA gain, $v_W(i)$ is the pulse waveform in volts, N is the number of the waveform samples, and Δt_S = 1 ns is the sampling time interval of the waveform digitizer. The calibration constant α was used to account for the uncertainties in the optical and electrical throughput measurements. It was determined from various GLAS calibration in orbit and was α=1.21 for the transmitted pulses and α=1.00 for the return pulses. The optical throughput for the transmitted laser pulses was 2.965 × 10^{-14} for Laser 1, 2.786×10^{-14} for Laser 2, and 2.793×10^{-14} for Laser 3. The optical throughput for the return laser pulses was 0.67. The VGA gain was roughly equal to $G=G_{tet}/255$ with G_{tel} an 8-bit integer given in the telemetry. A look-up table was used in the ground data processing to model the slight nonlinearity between the telemetry and the actual VGA gain.

The ICESat/GLAS surface reflectance measurement was calibrated early in the mission and was found to be accurate to about 10% when comparing the GLAS measurements with those from the independent methods using the runway at White Sands, New Mexico [26]. The GLAS reflectance measurements were recalibrated by comparing the ocean surface reflectance versus wind speed to a well-established model by Cox and Munk [27][28]. A series of minor corrections and fine adjustment were subsequently included in the ground data processing. The final GLAS surface reflectance measurements without saturation appeared to be accurate to better than 5% based on a 2006 ground calibration campaign at Railroad Valley, Nevada.

The GLAS surface reflectance measurement could be extended to include saturated echo pulses by correcting the saturation effect to the return pulse energy based the laboratory measurements shown in Fig. 10. A look-up table of return pulse energy correction as a function of raw pulse energy and the VGA gain was generated by numerically fitting a surface to the laboratory test data over the region of interest, as shown in Fig. 20. A return pulse energy correction satNrgCorr has been included in the GLAS data product since Release 28. It should be added to the raw pulse energy before calculating the surface reflectance [29]. Though lacking direct calibration with respect to ground truth, the GLAS surface reflectance and the corrected apparent surface reflectance measurements are consistent with naturally occurring surface reflection and atmosphere transmission variations [7] [17] [18] [19].

ACKNOWLEDGMENT

We would like to acknowledge the GLAS Science Team Leader, the late Robert Schutz, for his leadership of the ICESat mission. We thank the ICESat Project Scientist H. Jay Zwally for his continued support to this work, and the GLAS Science Team for their characterization of saturation effects on the GLAS measurements, in particular, David Hancock, Anita Brenner, and Christopher Shuman. We thank Peggy Jester for conducting the special operations of GLAS over the salar de Uyuni and other calibration sites, and Claudia Carabajal and Katy Quinn and for their participation in the salar de Uyuni surveys. We also thank James Spinhirne for providing data on the surface reflectance calibrations.

REFERENCES AND FOOTNOTES

[1] H. J. Zwally, B. Schutz, W. Abdalati J. Abshire, C.

Bentley, A. Brenner, J. Bufton, J. Dezio, D. Hancock, D. Harding, T. Herring, B. Minster, K. Quinn, S. Palm, J. Spinhirne, and R. Thomas, "ICESAT's laser measurement of polar ice, atmosphere, ocean, and land," *J. Geodynamics*, vol. 34, pp. 405-445, 2002.

[2] R. E. Schutz, H. J. Zwally, C. A. Schuman, D. Hancock, and J. P. DiMarzio, "Overview of the ICESat mission," *Geophys. Res. Lett.*, vol. 32, pp. L21S01-1 to L21S01-4, 2005.

[3] X. Sun, J. B. Abshire, J. F. McGarry, G. A. Neumann, J. F. Cavanaugh, J. C. Smith, D. J. Harding, H. J. Zwally, D. E. Smith, and M. T. Zuber, "Space lidar developed at NASA Goddard Space Flight Center The first 20 years," *IEEE Sel. Topics Appl. Earth Obs. Remote Sen.*, vol. 6, pp. 1660-1675, 2013.

[4] X. Sun,P. L. Jester,J. B. Abshire, and E. S. Chang, "Performance of the GLAS space lidar receiver through its seven-year space mission,' in *Proc. CLEO,* 2011 Paper ATuA2.

[5] H. J. Zwally and B. E. Schutz, *Results from Ice, Cloud and Land Elevation Satellite (ICESat) Mission*, Reprinted from *Geophys. Res. Lett.*, vol. 32, no. 21-23, 2005.

[6] J. B. Abshire, X. Sun, H. Riris, J. M. Sirota, J. F. McGarry, S. Palm, D. Yi, and P. Liiva, "Geoscience Laser Altimeter System (GLAS) on the ICESat mission: On-orbit measurement performance," *Geophys. Res. Lett.*, vol. 32, pp. L21S02-1 to L21S02-4, 2005.

[7] J. D. Spinhirne, S. P. Palm, W. D. Hart, D. L. Hlavka, and El. J. Welton, "Cloud and aerosol measurements from GLAS: Overview and initial results," *Geophys. Res. Lett.*, vol. 32, pp. L22S02-1 to L22S02-4, 2005.

[8] X. Sun, J. B. Abshire, D. Yi, and H. A. Fricker, "ICESat receiver signal dynamic range assessment and correction of range bias due to saturation," *EOS. Trans. AGU*, vol. 86, 2005 Fall Meet. Suppl., Abstract C234A-07.

[9] H. A. Fricker, A. Borsa, B. Minster, C. Carabajal, K. Quinn, and B. Bill, 'Assessment of ICESat performance at the salar de Uyuni, Bolivia,' *Geophys. Res. Lett.*, vol. 32, pp. L21S06-1 to L21S06-4, 2005.

[10] National Snow and Ice Data Center. "ICESat/GLAS Data: Description of Past Data Releases" last retrieved from http://nsidc.org/data/icesat/past_releases.html on April. 1, 2017.

[11] X. Sun, J. B. Abshire, M. A. Krainak, J. D. Spinhirne, S. P. Palm, R. S. Lancaster, and G. R. Allan, "Cloud and aerosol lidar channel design and performance of the Geoscience Laser Altimeter System on the ICESat mission," in *Proc. CLEO*, 2004, Paper CThT16.

[12] R. Measures, *Laser Remote Sensing: Fundamentals and Applications*, Krieger Publishing: New York, 1992.

[13] C. S. Gardner, "Target signatures for laser altimeters: an analysis," *Appl. Opt.*, vol. 21, pp. 448-453, 1982.

[14] C. S. Gardner, "Ranging performance of satellite laser altimeters," *IEEE Geosci. Remote Sens.*, vol. 30, pp. 1061-1072,1992.

[15] J. D. Spinhirne and S. P. Palm, "Global laser pulse reflectance at 1064 nm of snow and land surfaces from the GLAS satellite Lidar," *IEEE International Geoscience and Remote Sensing Symposium (IGARSS)*, pp. 646-648, 2010.

[16] F. G. Smith, editor, *Atmospheric Propagation of Radiation*, *IR/EO Systems Handbook*, SPIE Press, Bellingham, 1993, p.109.

[17] C. C. Carabajal, D. J. Harding, C. A. Schuman, and V. P. Suchdeo. "Laser altimeter mission design constraints from ICESat observation of 1064 nm apparent surface reflectance," *American Geophysical Union, Fall Meeting 2007*, Abstract G54A-04.

[18] D. Harding, "Pulsed laser altimeter ranging techniques and implications for terrain mapping," in *Topographic Laser Rangingand Scanning: Principles and Processing*, J. Shan and C. Toth, eds., CRC Press, Taylor & Francis Group, pp. 173-194, 2009.

[19] Y. Yang, A. Marshak, S. P. Palm, Z. Wang, and C. Schaaf, "Assessment of cloud screening with apparent surface reflectance in support of the ICESat-2 mission," *IEEE Trans. Geoscience and Remote Sensing*, vol. 51, pp. 1037-1045, 2013.

[20] A. A. Borsa, H. A. Fricker, B. G. Bills, J.-B. Minster, C. C. Carabajal, and K. J. Quinn, "Topography of the salar de Uyuni, Bolivia from kinematic GPS," *Geophysics Journal International*, vol. 172, pp. 31-40, 2008.

[21] K. M. Brunt, A. A. Borsa, and H. A. Fricker, "Repeated GPS surveys of the salar de Uyuni for continued calibration of ICESat altimeter data," *2009 Fall AGU meeting*, Paper G53A-0668.

[22] A. A. Borsa, "Validation of CryoSat-2 LRM and SARIN-mode elevations over the salar de Uyuni, Bolivia," *Cryosat User Workshop 4, ESA Living Planet Symposium*, 9-13 May 2016

[23] A. A. Borsa, G. Moholdt, G., H.A. Fricker, and K.M. Brunt, "A range correction for ICESat and its potential impact on ice-sheet mass balance studies," *The Cryosphere*, vol. 8, no. 2, pp. 345-357, 2014.

[24]. S. P. Palm, Y. Yang, J. D. Spinhirne, and A. Marshak, "Satellite remote sensing of blowing snow properties over Antarctic," J. Geophysical Research, vol. 116, pp. D16123, 2011.

[25] B. Hapke, *Theory of Reflectance and Emittance Spectroscopy*, Cambridge University Press, Cambridge, 1993, Ch. 8.

[26] K. Thome, J. Reagan, J. Geis, M. Bolt, and J. Spinhirne, "Validating of GLAS calibration using ground- and satellite-based data," *Geoscience and Remote Sensing Symposium (IGARSS), 2004 IEEE International*, vol. 4, pp. 2468-2471.

[27] C. Cox and W. Munk, "Measurement of roughness of the sea surface from photographs of the Sun's glitter," *J. Opt. Soc. Am*, vol. 44, pp. 838- 850, 1954.

[28] R.S. Lancaster, J.D. Spinhirne, and S.P. Palm, "Laser pulse reflectance of the ocean surface for the GLAS satellite lidar," *Geophys. Res. Lett.*, vol. 32, pp. L22S10-1 to L22S10-4, 2005.

[29] GSAS v5.4 Release Notes, June 25, 2008 http://nsidc.org/sites/nsidc.org/files/files/gsas_v5_4_release.pdf

Xiaoli Sun (S'88-M'90) received the B.S. degree from Taiyuan Institute of Technology, Taiyuan, China, in 1982, and the Ph.D. degree in electrical engineering from the Johns Hopkins University, Baltimore, MD, USA, in 1989. He is now a Research Physical Scientist in the Solar System Exploration Division at the NASA Goddard Space Flight Center, Greenbelt, MD, USA. He was the Lead Engineer in the photodetector development and receiver performance analysis for the Mars Orbiter Laser Altimeter on the Mars Global Surveyor Mission and the Geoscience Laser Altimeter System on the ICESat Mission. He was the instrument scientist for the Mercury Laser Altimeter on the MESSENGER mission, the Lunar Orbiter Laser Altimeter, and the Laser Ranging system on the Lunar Reconnaissance Orbiter (LRO) mission. He led the first two-way laser ranging experiment between the MESSENGER spacecraft and Earth over 24 million km in 2005, and the first lunar laser communication experiments from Earth to LRO at lunar distance in 2012. He is the lead research scientist for infrared lidar detector development and receiver modeling for trace gas lidar at NASA Goddard Space Flight Center, such as the CO_2 lidar for NASA's Active Sensing of CO_2 Emission over Nights, Days, and Seasons (ASCENDS) mission.

James B. Abshire (S73-M81- SM85) is the Senior Scientist for Laser Remote Sensing for the Solar System Exploration Division at NASA's Goddard Space Flight Center. He has helped lead the development of space lidar at Goddard, and was Instrument Scientist on the Mars Orbiter Laser Altimeter on the Mars Global Surveyor Mission and the Geoscience Laser Altimeter System on the ICESat Mission. He currently is leading Goddard's work in remotely measuring atmospheric CO_2 with lidar and serves on the formulation teams for the NASA ASCENDS mission and the French/German MERLIN mission. He received his Ph.D. in Electrical Engineering from the University of Maryland in 1982, and B.S. in Electrical Engineering from the University of Tennessee in 1974. He is a member of the IEEE, Optical Society of America, and the American Geophysical Union.

Adrian A. Borsa is an assistant professor at the Institute of Geophysics and Planetary Physics at the Scripps Institution of Oceanography. His work aims to describe how the shape of Earth's surface is changing at timescales of seconds to decades, and to link observed change to geophysical processes associated with phenomena ranging from earthquakes to climate change. Dr. Borsa's expertise includes the collection and analysis of geodetic data from many sources, including permanent and mobile GPS sensors, airborne lidar, and satellite altimeters. He is also actively involved in the calibration and validation of elevation measurements from several generations of satellite altimeters, and has made the remote salar de Uyuni in Bolivia his field home for the past decade in support of this work.

Helen Amanda Fricker is a Professor in the Institute of Geophysics and Planetary Physics at Scripps Institution of Oceanography, UCSD. Her research focuses on ice sheets in Antarctica and Greenland and their role in the climate system. She uses a combination of satellite radar and laser altimetry and other remote-sensing data to understand ice sheet processes. Professor Fricker is widely recognized for her discovery of active sub-glacial lakes, and she has shown that these lakes form dynamic hydrologic systems, where one lake can drain into another in a short period of time. She is also known for her innovative research into Antarctic ice shelf mass budget processes such as iceberg calving and basal melting and freezing. Fricker received the Martha Muse Prize for Science and Policy in Antarctica from SCAR in 2010. Fricker was a member of the ICESat Science Team. She is on the ICESat-2 Science Definition Team and the NASA Sea Level Change Team.

Donghui Yi received the B.S. degree in geophysics and the M.S degree in atmospheric physics from Peking University, Beijing, China in 1986 and 1989, respectively, and the Ph.D. degree in geophysics from the University of Wisconsin-Madison, Madison, WI, USA in 1996. He worked as a Research Associate at the University of California-San Diego for a year and joined NASA's ICESat program in 1997 and Operation IceBridge program in 2011. He is currently a Chief Scientist at SGT Inc. with NASA's Cryospheric Sciences Laboratory, Goddard Space Flight Center, Greenbelt, MD, USA. His primary research interests include laser and

radar altimetry data analysis, algorithm development, and applying altimetry data for sea ice, ice sheet, and lake study over the Arctic, Antarctic, and Himalaya regions. Dr. Yi is a member of the American Geophysical Union and a member of the International Glaciological Society.

John P. DiMarzio received the B.S. degree in physics from the University of Maryland, College Park, in 1990. He has been extensively involved in satellite radar and laser altimetry since 1989 and is currently a Chief Systems Engineer for Stinger Ghaffarian Technologies (SGT), Inc., Greenbelt, MD, on a National Aeronautics and Space Administration (NASA)/Goddard Space Flight Center contract supporting the ICESat mission and satellite radar altimetry studies. He has six referred publications using altimetry for studying the ice sheets. Mr. DiMarzio is a member of the American Geophysical Union. He has received NASA Group Achievement Awards for supporting the ICESat mission.

Fernando S. Paolo is a postdoctoral scholar at the Institute of Geophysics & Planetary Physics at the Scripps Institution of Oceanography. Fernando's research interests include the use of multiple satellite altimeters to study how the Antarctic and Greenland ice sheets are changing, and the implications for future sea-level rise. He is particularly interested in understanding the large-scale oceanic and atmospheric processes causing ice-sheet mass loss through interaction with the Antarctic ice shelves. Fernando received a B.S. in Oceanography and an M.S. in Geophysics from the University of São Paulo, Brazil. He then moved to the U.S. where he received his Ph.D. in Geophysics from the Scripps Institution of Oceanography / University of California, San Diego in 2015.

Kelly M. Brunt is an Associate Research Scientist with the Earth Science Interdisciplinary Center (ESSIC), at the University of Maryland. She is located at NASA where she joined the Cryospheric Sciences Laboratory in June 2010. She obtained a B.S. in Geology from Syracuse University and an M.S. in Geology from the University of Montana. She received her Ph.D. degree in Geophysics from the University of Chicago in 2008, modeling ice-shelf flow and the connection between ice shelves, ice streams, and the ocean. As a postdoctoral scholar at Scripps Institution of Oceanography, she worked on the calibration and validation of Ice, Cloud, and land Elevation Satellite (ICESat) laser altimetry data. Dr. Brunt is currently working on the planning for the post-launch calibration and validation of ICESat-2 elevation data. She is also working with MABEL, a high-altitude airborne laser altimeter designed as a simulator for ICESat-2.

David J. Harding received the B.S. and Ph.D. degrees in geological sciences from Cornell University, Ithaca, NY, USA, in 1980 and 1988. Since 1991, he has been a Research Scientist with the NASA Goddard Space Flight Center, Greenbelt, MD, USA, as a member of the Planetary Geodynamics Laboratory in the Sciences and Exploration Directorate. As of 2017 he is a member of the Biospheric Sciences Laboratory. He conducts research in the topographic expression of land surface processes, the structure of vegetation and the physical properties of snow, ice and water, in particular by developing and utilizing advanced airborne and spaceflight laser altimeter systems. He is the principal investigator for the airborne Slope Imaging Multi-polarization Photon-Counting Lidar (SIMPL). Dr. Harding was a member of the Ice, Cloud and land Elevation Satellite (ICESat) Science Team and ICESat-2 Science Definition Team.

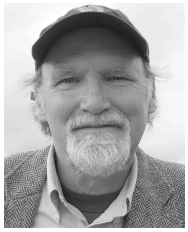

Gregory A. Neumann received the B.A. degree in mathematics from Reed College, Portland, OR, USA, in 1969 and the M.S. and Ph.D. degrees in geological sciences from Brown University, Providence, RI, USA, in 1991 and 1993, respectively. From 1993 to 2005 he was a Research Scientist at The Johns Hopkins University and the Massachusetts Institute of Technology. Since 2005 he has been a geophysicist at the NASA Goddard Space Flight Center, Greenbelt, Maryland. He has led the analysis of laser altimetry from the Clementine, Mars Global Surveyor, NEAR-Shoemaker, MESSENGER, and Lunar Reconnaissance Orbiter missions as well as participating in the DAWN and GRAIL missions. He specializes in the use of laser altimetry, sonar bathymetry, gravity, and magnetics to interpret planetary crustal structure. He has authored and co-authored more than 90 journal articles and has produced graphics from planetary topography for popular magazines and textbooks. Dr. Neumann has received the 2011 Robert H. Goddard award for Scientific Achievement and numerous other NASA awards. He has been a member of the American Geophysical Union since 1982.

Tables

Table I: Selected ICESat/GLAS campaign metadata.

Laser	Campaign	Start date	# Days	Mean Transmit Energy (mJ)	Min/Max Transmit Energy (mJ)	Median Transmit Power (mJ)
Laser 1	L1a	2/20/03	29	66.9	51 - 72	67.7
	L1b	3/21/03	8	55.5	51 - 72	55.7
Laser 2	L2a	9/25/03	37	68.0	55 - 80	68.4
	L2b	2/17/04	33	43.1	33 - 57	41.7
	L2c	5/18/04	34	13.3	5 - 33	10.9
Laser 3	L3a	10/3/04	36	63.1	62 - 67	64.1
	L3b	2/17/05	35	59.6	54 - 69	59.8
	L3c	5/20/05	34	46.1	44 - 49	45.7
	L3d	10/21/05	34	39.9	39 - 43	39.8
	L3e	2/22/06	34	34.2	30 - 39	34.4
	L3f	5/24/06	33	31.2	30 - 33	31.2
	L3g	10/25/06	33	27.2	24 - 31	27.1
	L3h	3/12/07	33	22.9	22 - 24	22.7
	L3i	10/2/07	34	20.6	20 - 22	20.5
	L3j	2/17/08	33	17.8	16 - 21	17.7
	L3k	10/4/08	15	15.6	12 - 17	16.2
Laser 2	L2d	11/25/08	22	5.3	4.5 - 8	5.4
	L2e	3/9/09	33	2.9	2 - 6	2.4
	L2f	9/30/09	11	3.3	2.5 - 4	3.2

Table II: GLAS instrument design parameter values.

Laser pulse energy	70 mJ
Pulse repetition rate	40 Hz
Pulse width	6 ns FWHM
Wavelength	1064.50 ±0.1 nm
Beam divergence	110 μrad full angle at e^{-2} points
Receiver aperture	1.0 m diameter
Receiver field of view	500 μrad
Receiver optics transmission	68%, with bandpass filter and secondary mirror
Receiver optical bandwidth	0.8 nm FWHM
Detector electrical bandwidth	140 MHz
Noise equivalent power	40 fW/Hz$^{1/2}$
Waveform digitization	1 GHz at 8 bits
Digital filter impulse FWHM	4, 8, 16, 32, 64, 128 ns (Gaussian pulse shape)

Table III: ICESat/GLAS passes across the salar de Uyuni with sufficient signal dynamic range to verify and refine the saturation correction algorithm (see Fig. 12 for ground track location.

Campaign	Track	Date	VGA Gain Range
Laser 3a	360	11/2/2004	13
Laser 3b	360	2/30/2005	13
Laser 3e	085	3/5/2006	13-61
Laser 3h	085	3/22/2007	13-71
Laser 3e	360	3/23/2006	26
Laser 3h	360	4/10/2007	80
Laser 3g	360	11/23/2006	128

Table IV: Results of the curve fit of range bias correction for variable gain amplifier (VGA) gain 13, 26, 80, and 125.

VGA Gain, G	$E_{th}(G)$	$\alpha(G)$
13	9.00	1.33
26	5.30	0.70
80	4.40	0.29
128	2.10	0.15

Table V: Coefficients of the curve fits to the laboratory test data and the salar de Uyuni data for use in (5) and (6). The parameters with updated values using the salar de Uyuni data fit are given in boldface font.

Coefficients	Laboratory Test	salar de Uyuni
a_0	0.250	0.250
b_0	0.0625	0.0625
c_1	0.240	**0.250**
c_2	9.90	**9.00**
c_3	18.0	18.0
c_4	4.50	**3.50**
c_5	0.300	0.300
c_6	0.0250	**0.0100**
c_7	1.56	**0.980**
c_8	15.0	**18.0**
c_9	4.50	**4.00**
c_{10}	0.300	**0.0120**

Figures

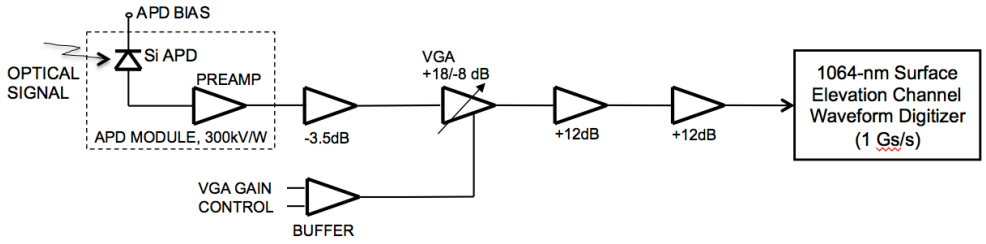

Fig. 1: Block diagram of the GLAS 1064-nm altimetry channel receiver electronics, showing the Si APD (silicon avalanche photo diode), VGA (variable gain amplifier), and waveform digitizer.

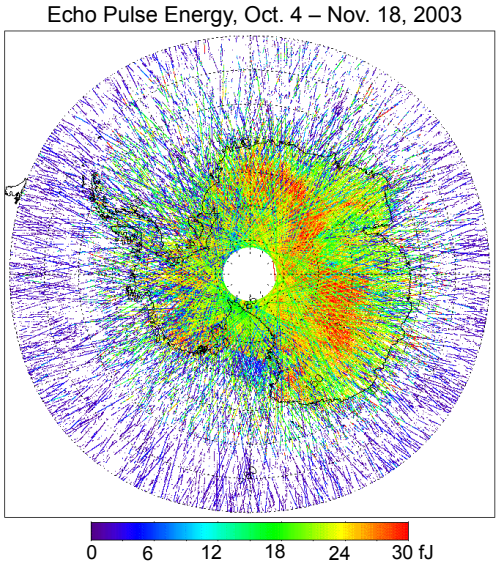

Fig. 2: GLAS return pulse energy from campaign Laser 2a over Antarctica, showing wide signal dynamic range and high energies from the flat high-elevation ice sheet interior.

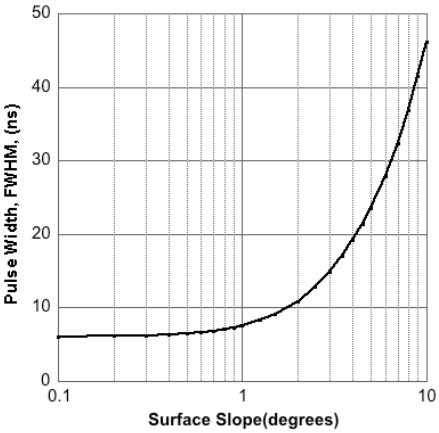

Fig. 3: Calculated GLAS return pulse width (FWHM, or full-width at half-maximum) as a function of the surface slope using the nominal instrument parameter values given in Table II and assuming a smooth and planar ground surface.

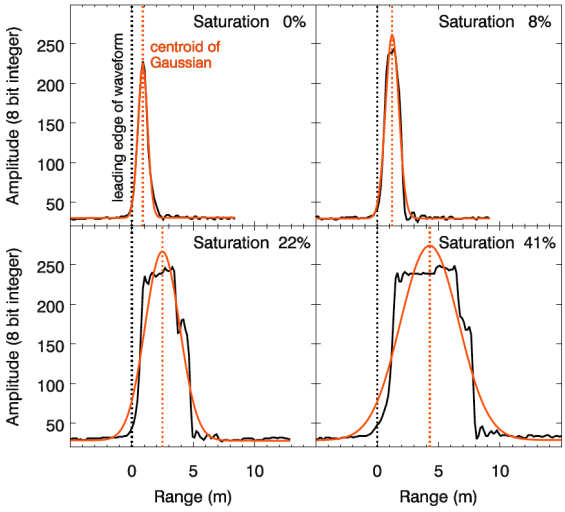

Fig.4: GLAS return waveforms (black curves) and accompanying Gaussian fits (orange curves) from the salar de Uyuni, Bolivia, for a single pass during campaign Laser 3e. Patchy water on the surface resulted in a wide range of return signal power and receiver saturation. The progression between the figure panels (from 0% to 41% saturation) shows that the centroid of the Gaussian fit to the return waveform moved to longer ranges with higher saturation, even though the surface elevation was nearly unchanged.

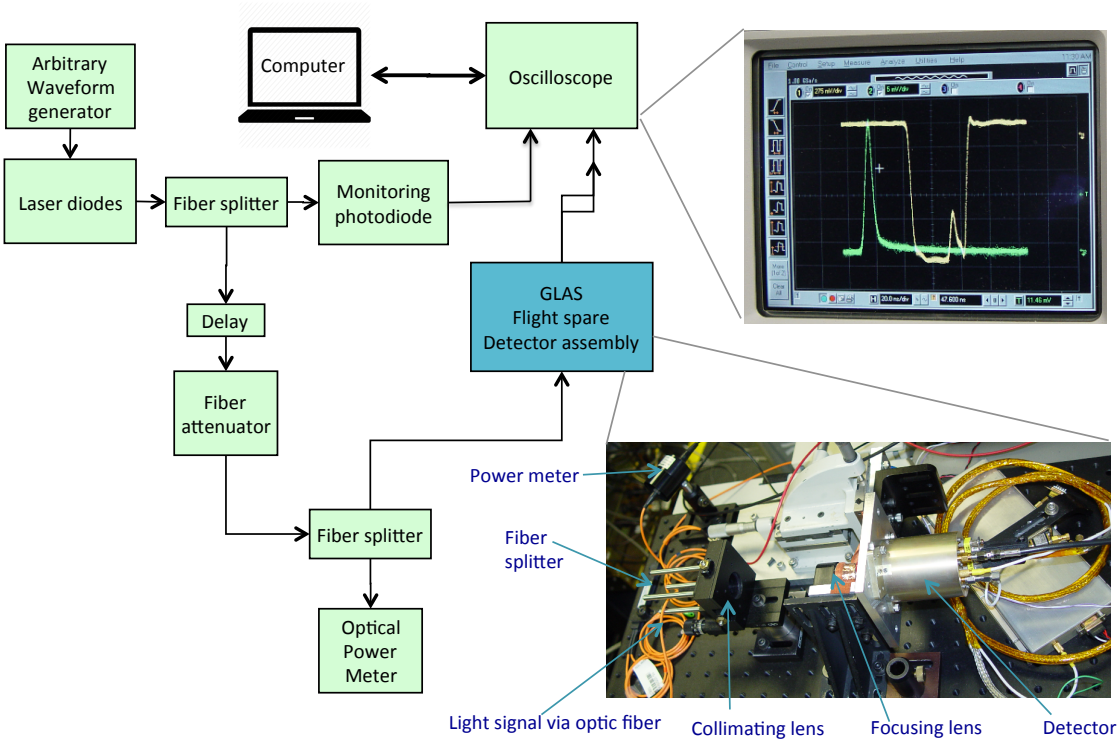

Fig. 5: Laboratory test setup using the GLAS flight spare detector to characterize receiver saturation.

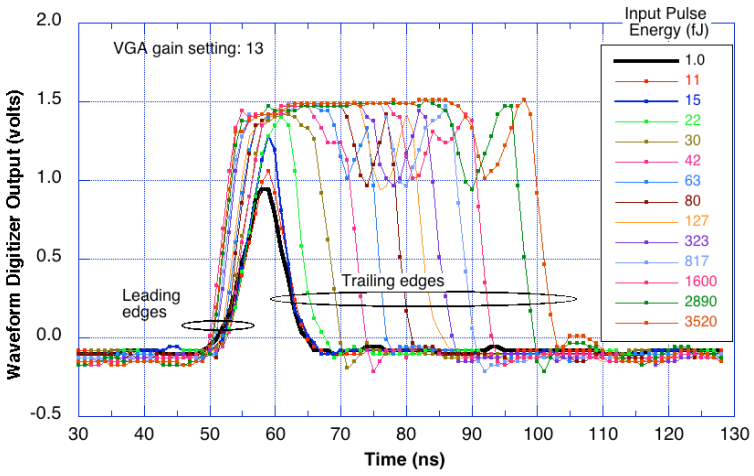

Fig. 6: Sample pulse waveforms output from the GLAS flight spare detector at different input laser energy levels. The input laser pulse width was 6 ns FWHM. The VGA gain setting was 13, which was the same as the preset lower limit in the GLAS telemetry units.

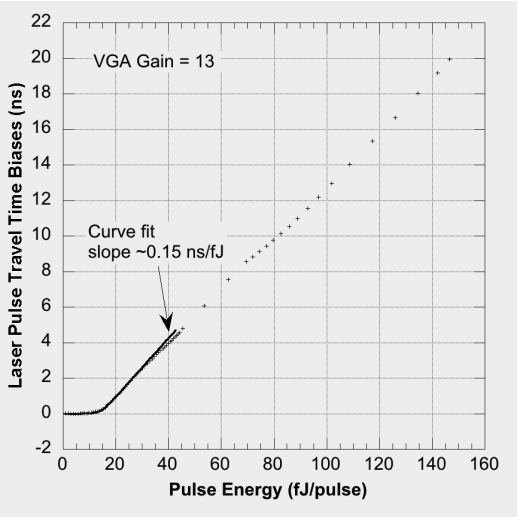

Fig. 7: Travel time bias due to saturation as a function of pulse energy at VGA gain 13. The time bias was calculated by differencing the location of the peaks of the Gaussian fits to the return pulses in reference to the transmitted laser pulses. A constant time offset has been subtracted to show the time bias due to saturation. Also shown is a curve fit to the measurement data for energies of 0 to 40 fJ/pulse, where most of the saturation occurred.

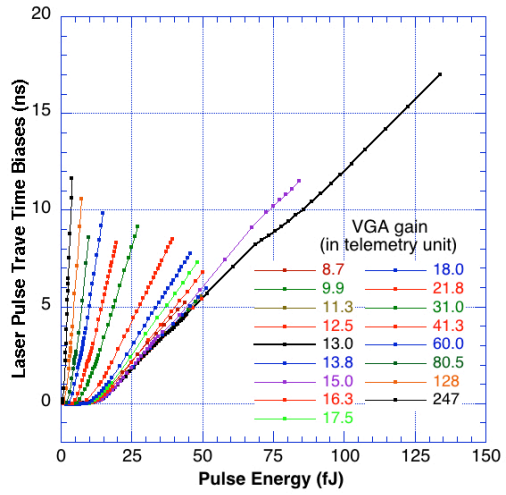

Fig. 8: Pulse travel time bias due to saturation for a range of VGA gain settings. For a given pulse energy, the pulse travel time biases decreased with VGA gain for gain < 13 and increased with VGA gain for gain > 13.

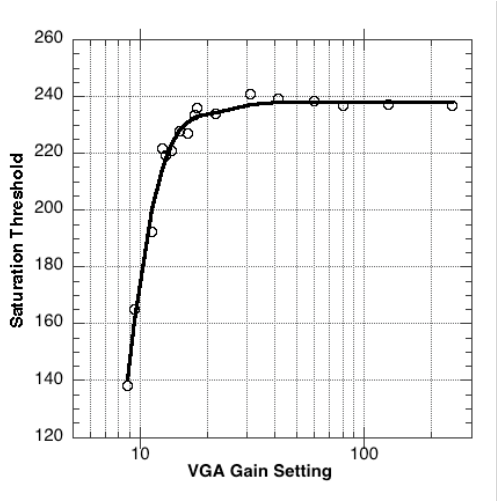

Fig. 9: Digitizer waveform saturation thresholds (in unitless counts within the range 0–255) for a range of VGA gain settings (open circles). The black line is a piecewise curve fit obtained from (3).

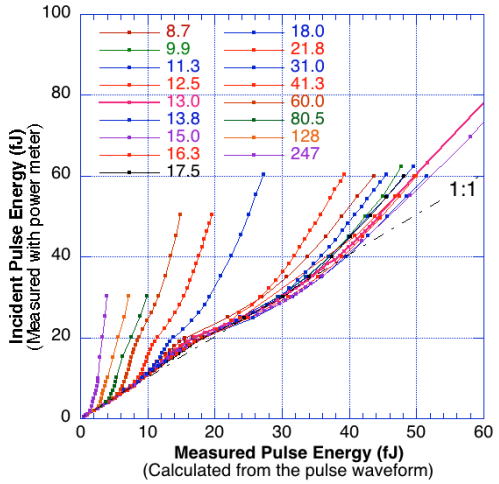

Fig. 10: Actual laser pulse energy vs. energy estimated from Gaussian fits to the return pulse waveforms, for the same range of VGA gains shown in Fig. 9.

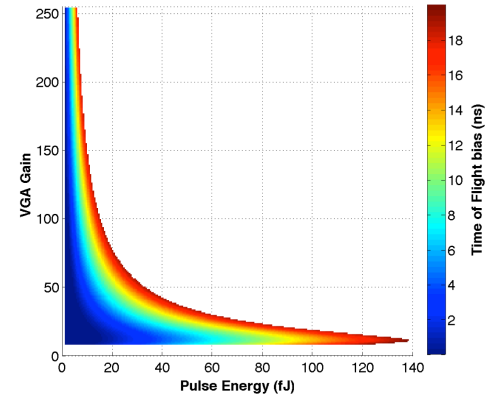

Fig. 11: Travel time bias due to saturation as a function of pulse energy and VGA gain, derived from the laboratory tests described in the text.

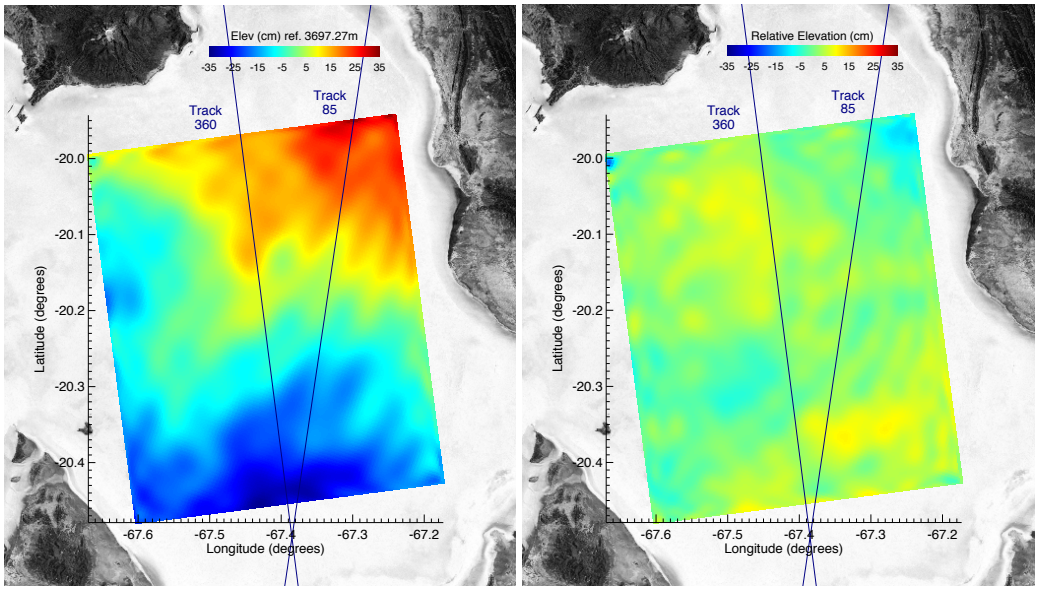

Fig. 12: (a) Digital Elevation Model (DEM) of the salar de Uyuni, Bolivia constructed from 2002 GPS survey data. Black lines are the ICESat/GLAS ground tracks for Tracks 85 and 360. (b) Change in the surface elevation of the salar de Uyuni between 2002 and 2009. Background image in both cases is from Landsat.

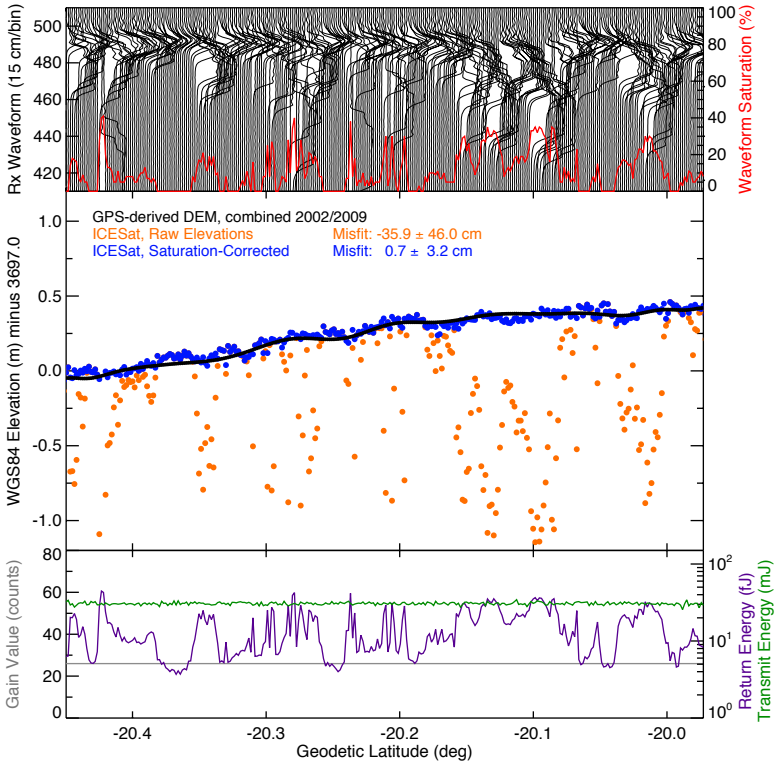

Fig. 13: Summary of validation data from the salar de Uyuni for campaign Laser 3e, Track 360 on March 23, 2006. The return pulse waveforms in the top panel correspond to the elevations in the middle panel and the gain/energy values in the bottom panel, where the VGA gain was held constant at a value of 26. Orange points in the middle panel are raw GLAS elevations, blue points are saturation-corrected GLAS elevations, and the black line shows the corresponding GPS reference elevation for Track 360. All data shown are from Release 34 of the ICESat dataset.

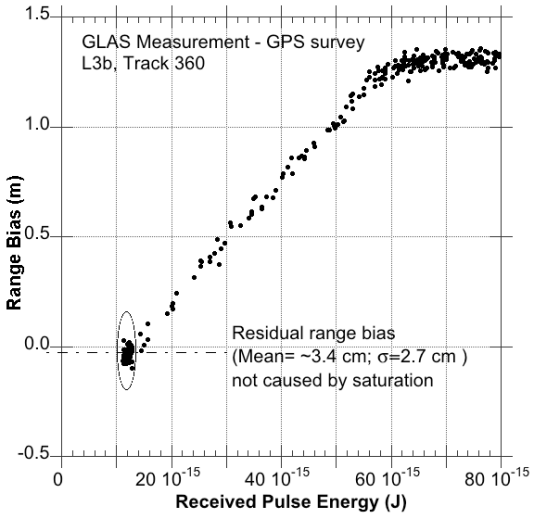

Fig. 14: ICESat/GLAS range bias derived from the GPS survey over the salar de Uyuni for campaign Laser 3b, Track 360.

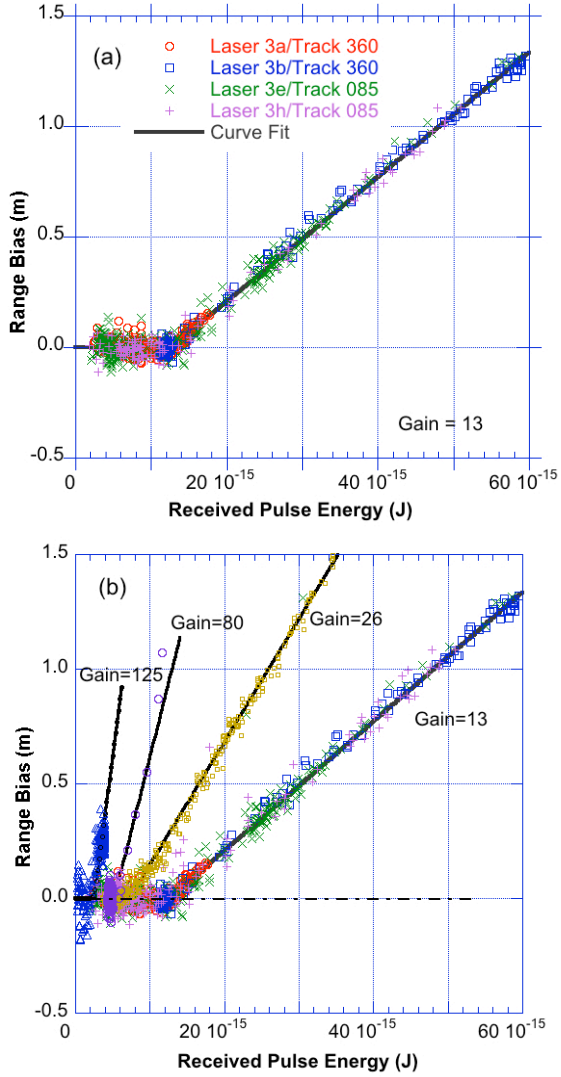

Fig. 15: (a) ICESat/GLAS range bias for VGA gain 13, campaigns Laser 3a, Laser 3b, Laser 3e and Laser 3h; (b) Range bias at VGA gain 13, 26, 80, and 125. Fits to these data from (4) are also plotted.

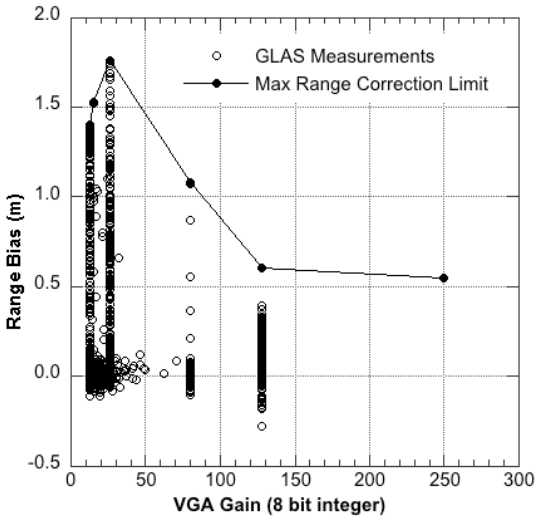

Fig. 16: ICESat/GLAS range bias from the salar de Uyuni for campaigns Laser 3a, Laser 3b, Laser 3e, Laser 3g, and Laser 3h along with the corresponding upper limit (the maximum valid range correction) for the saturation correction.

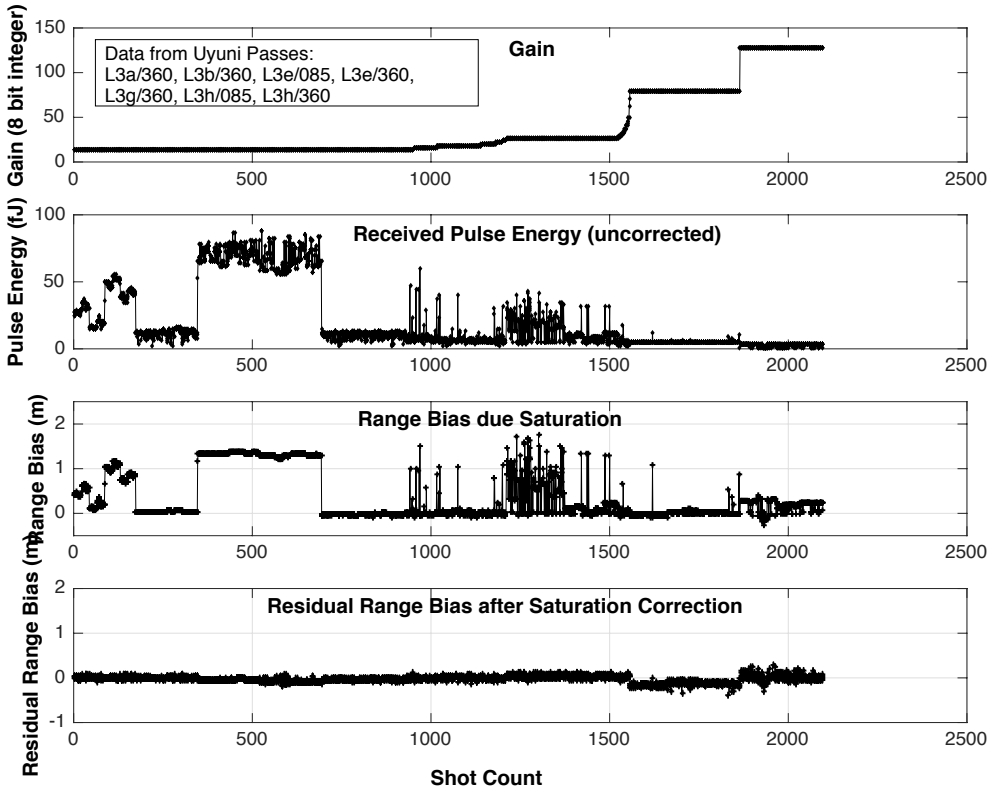

Fig. 17: VGA gain, received (return) pulse energy, and range bias for the seven salar de Uyuni passes, and the residual range bias after applying the saturation correction.

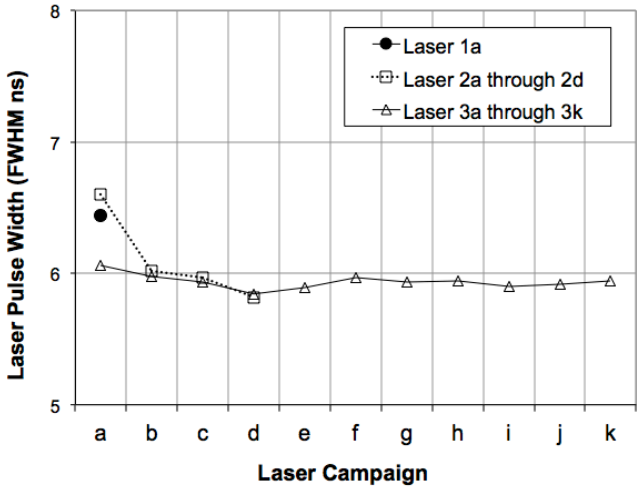

Fig. 18: Average GLAS laser pulse width for 16 laser campaigns (Laser 1 to Laser 2d).

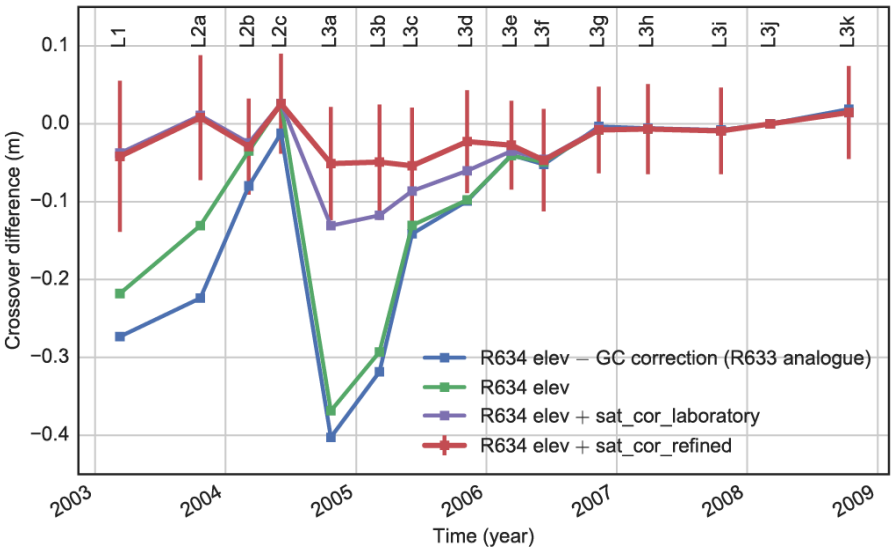

Fig. 19: Crossover elevation biases between each campaign and Laser 3j (not saturated) over the central East Antarctic Ice Sheet. The curves are: biases without any correction applied, i.e., the GC correction has been removed from the Release 34 (R634) data to simulate Release 33 (R633) data (blue); biases with the GC correction only (green); biases with the GC and laboratory-based saturation correction (purple); and biases with the GC and refined saturation correction (red). Error bars are one standard deviation, displayed only for the optimally corrected data (red curve) to avoid cluttering the figure.

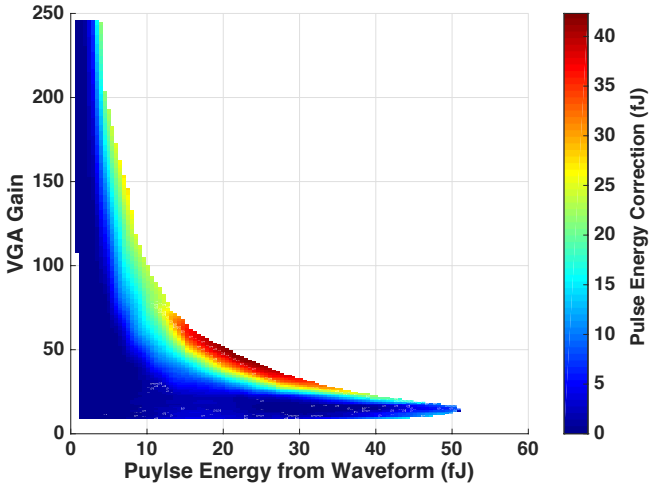

Fig. 20: Return pulse energy correction as a function of pulse energy and VGA gain. The value of the energy correction is included in the data product and should be added to the raw pulse energy before calculating surface reflectance.